Wave Inversion Technology, Report No. 2, pages 7-24

The Common Reflection Surface Stack – Part I: Theory

G. Höcht, J. Mann, R. Jäger[1]

keywords: *model independent imaging, zero-offset simulation*

ABSTRACT

The simulation of a zero-offset (ZO) section from multi-coverage reflection data for 2-D media is a widely used seismic reflection imaging method that reduces the amount of data and enhances the signal-to-noise ratio. The aim of the CRS stack method is not only to improve the resulting stack section but also to determine parameters that are useful with respect to a subsequent inversion. The main advantage of the common reflection surface (CRS) stack is the use of analytical formulae that describe the kinematic reflection response of inhomogeneous media with curved interfaces but do not depend on a macro velocity model.

For the travel time estimation the CRS stack uses circular wavefronts that are associated with the local dips and radii of curvatures of the reflectors. The result of this approach yields a stacking surface in the data set for each point in the simulated ZO section. These concepts are based on ideas of de Bazelaire (1986), de Bazelaire and Thore (1987), Gelchinsky (1988), Keydar et al. (1990) and Berkovitch et al. (1994). However, we give no review of their methods but use a different approach for the derivation of the formulae involved in the CRS stack.

For constant velocity media we derive exact formulae for the CRS stack. In order to extend these formulae to inhomogeneous media we use attributes of hypothetical waves that would be observed at the surface (Hubral (1983)). The resulting formulae depend on these a priori unknown attributes, which can be determined by a search procedure involving coherency analysis (Taner and Koehler (1969)).

Besides the stack section, one obtains a coherency section and various attribute sections. The coherency section is helpful to identify the locations of reflection events. There, one can subsequently use the attributes to derive the a priori unknown macro velocity model (Hubral and Krey (1980), Goldin (1986)).

Taylor series expansions of the CRS surface provide explicit formulae. Additionally, these formulae allow to split the search procedure into separate steps in order to reduce the computational costs: e. g., the search of the required attributes can be first performed in the CMP gathers and afterwards in the resulting CMP stack section, a concept introduced by de Bazelaire and Thore (1987).

[1]**email:** ghoecht@gpiwap4.physik.uni-karlsruhe.de

INTRODUCTION

Seismic reflection imaging is the objective of a multitude of methods with a wealth of illustrations in order to "illuminate" the data. In this context, a "unified approach" is described by Hubral et al. (1996a) and Tygel et al. (1996). An important seismic reflection imaging process that is widely applied in practice is the simulation of a ZO section from a set of common-offset (CO) sections. To this category of seismic imaging one counts standard seismic reflection methods such as the well-known common-midpoint (CMP) stack and the normal moveout/dip moveout (NMO/DMO) stack (Black et al. (1995), Höcht et al. (1997)), which is also called migration to zero-offset (MZO) (Hubral et al. (1996b)). The resulting stack section can subsequently be post-stack depth migrated to obtain an image of the subsurface. Another seismic reflection imaging method is the pre-stack depth migration (PSDM) that directly provides an image of the subsurface. However, these methods are either model dependent or based on assumptions that are not appropriate for complex media. Even for the constant velocity case, processes as the NMO/DMO stack and the PSDM cannot provide the best reflector illumination as discussed by Hubral et al. (1998). In contrast, approaches formulated by de Bazelaire and Thore (1987), de Bazelaire and Viallix (1994) or Berkovitch et al. (1994) are designed to handle complex media and additionally consider the reflectors' curvatures. Based on their ideas, we describe the kinematic reflection response of inhomogeneous media with curved interfaces through analytic formulae. These formulae are derived from a kinematic point of view meaning that neither the amplitudes nor possible phase shifts are considered.

In the following we assume that different CO sections have been acquired for the same seismic line. Each trace in a CO section shows the measured reflection events, which are provided by an experiment with a single shot/receiver pair, with respect to time t. A CO section is defined by the constant offset of a source/receiver pair. Thus, one can imagine a source/receiver pair to be shifted on the seismic line to provide different traces and thereby an entire CO section. We assume that each trace is plotted at the midpoint x_m between the corresponding shot/receiver pair such that a CO section describes a (x_m-t) domain. A CO section itself we specify by the half-offset h of a shot/receiver pair. The ZO section is the special case of a CO section with coincident shot/receiver pairs ($h = 0$).

For appropriate illustration the CO sections are arranged in a (t-x_m-h)-space, where t denotes the time, x_m the midpoint, and h the half-offset. Each point on the (x_m-h)-plane defines one shot/receiver pair and thereby a trace by its coordinates (x_m, h). For the corresponding experiment the source and receiver are located on the seismic line at $x_s = x_m + h$ and $x_g = x_m - h$, respectively. The CO travel time curves that stem from the same reflector together define a travel time surface in the (t-x_m-h)-space. Figure 3 shows an example of such an illustration in the (t-x_m-h)-space. A point in the ZO section for which the ZO simulation has to be performed is denoted by $P_0 = (x_0, t_0)$.

The reflection events in the data are the response of the subsurface to propagating waves that originate and are observed on the surface. However, for our kinematic approach it is more suitable to consider the associated rays, which we assume to be normal to the wavefronts. In this manner, one can associate each reflection event with a ray. This ray takes an appropriate path (determined by the ray parameter) in the subsurface to provide the (travel) time of the reflection event. In this context we define the ZO ray to be associated with a primary reflection event in the ZO section. In most cases this ray is normal to the reflector that generates this reflection event.

The proposed strategies can be applied to complex media but are in the presented form based on ZO rays with normal incidence on the reflector. Furthermore, the derived formulae that account for inhomogeneous media are, strictly speaking, only valid in the vicinity of the ZO ray. With regard to ray theory this concerns the paraxial rays of the (central) ZO ray.

CONSTANT VELOCITY MEDIA

To introduce the CRS stack, we use the constant velocity model shown in fig. 1. Let us assume that one has chosen the location $P_0 = (x_0, t_0)$ of a primary reflection event in the ZO section (see fig. 3). The coordinates of this point denote the location of the trace x_0 and the ZO travel time t_0. In addition, x_0 defines the location of the coincident shot/receiver pair. The corresponding ZO ray that connects the seismic line at x_0 with the reflection point R is shown in dark gray in fig. 2. In the following, we refer to this ZO ray as central ZO ray. In fig. 2 we have attached an arc segment C_R (shown in dark gray) to point R defined by the dip and radius of curvature of the reflector at R.

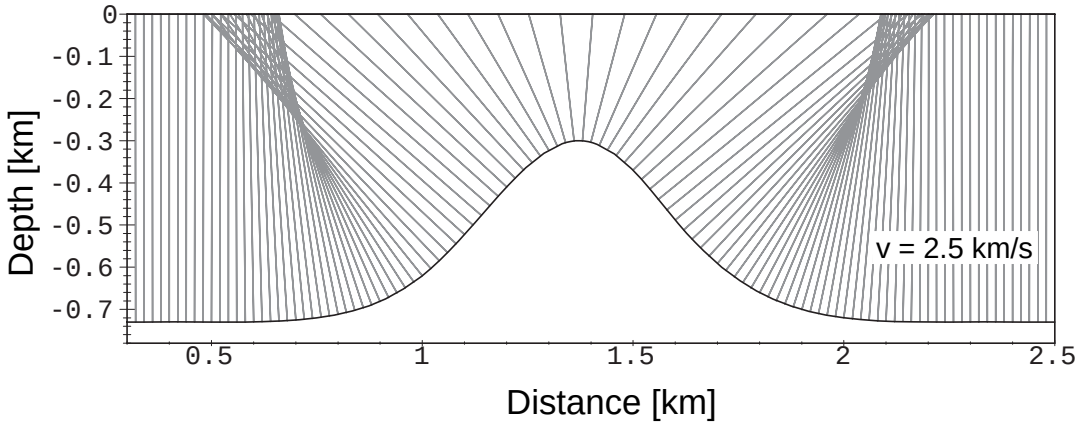

Figure 1: Constant velocity model: dome-like reflector. The corresponding ZO rays are depicted in gray.

Let us firstly determine the ZO traveltime $\tilde{t}_0$ and the emergence location $\tilde{x}_0$ of

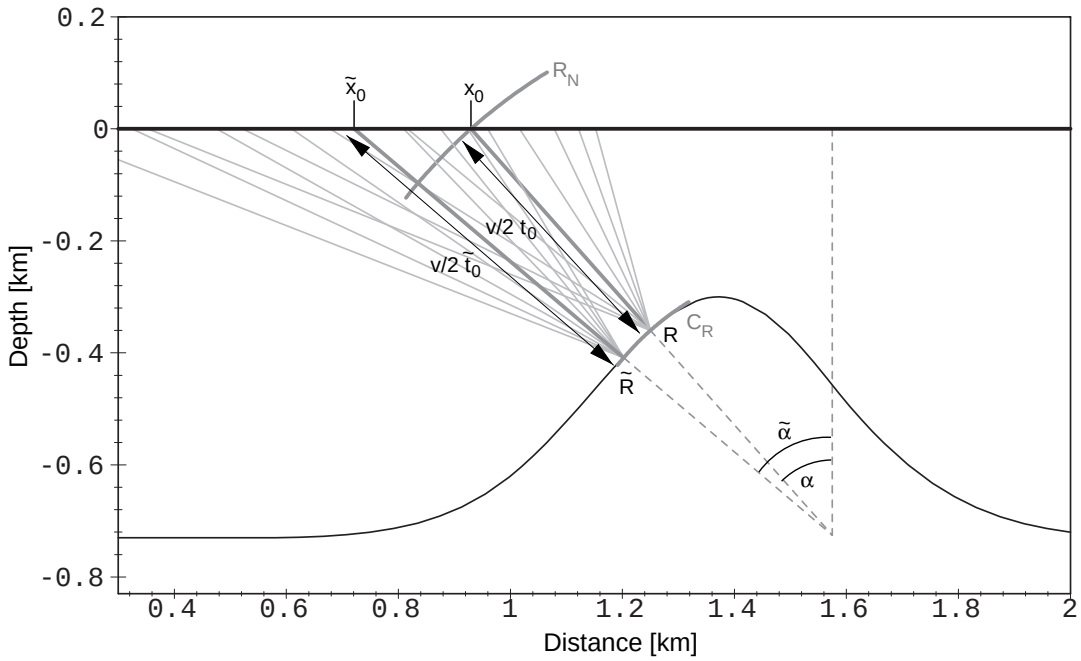

Figure 2: Constant velocity model: illumination of point $\tilde{R}$ and point R, both located on the circle C_R.

the respective ZO ray for an arbitrary point on the circular reflector specified by the (emergence) angle $\tilde{\alpha}$ (see fig. 2). The equations for $\tilde{t}_0(\tilde{\alpha})$ and $\tilde{x}_0(\tilde{\alpha})$ can be written in dependency of the coordinates of P_0 and attributes associated with the central ZO ray to P_0:

$$\tilde{x}_0(\tilde{\alpha}) = x_0 + R_N \left(\cos\alpha \, \tan\tilde{\alpha} - \sin\alpha\right) , \tag{1}$$

$$\tilde{t}_0(\tilde{\alpha}) = \frac{2}{v} R_N \left(\frac{\cos\alpha}{\cos\tilde{\alpha}} - 1\right) + t_0 , \tag{2}$$

$$\text{with} \quad R_N = R_R + \frac{v}{2} t_0 . \tag{3}$$

Here, α denotes the emergence angle of the central ray and R_R the radius of the circle C_R, i. e. the radius of curvature of the reflector at the reflection point R. Thus, knowing α and R_R of the reflector at R one can determine the ZO location $\tilde{x}_0$ and the ZO travel time $\tilde{t}_0$ for another point $\tilde{R}$ on the circle specified by the angle $\tilde{\alpha}$.

A CRP trajectory defines the locations of all primary reflection events in the (t-x_m-h)-space that pertain to the same reflection point on the reflector. The CRP rays for R and $\tilde{R}$ associated with the respective CRP trajectories are depicted in light gray in fig. 2. To compute the CRP trajectory for a point on the circle C_R (see fig. 2) we use the coordinate of a point ($\tilde{x}_0(\tilde{\alpha})$, $\tilde{t}_0(\tilde{\alpha})$) in the ZO section and the associated angle $\tilde{\alpha}$ as initial values (eqs. (1) and (2)). The CRP trajectory for each point $\tilde{R}$ on the circle

C_R is then given by the following formulae:

$$x_m(\tilde{\alpha}, h) = \tilde{x}_0(\tilde{\alpha}) + \tilde{r}_T \left(\sqrt{\frac{h^2}{\tilde{r}_T(\tilde{\alpha})^2} + 1} - 1 \right) , \quad (4)$$

$$t^2(\tilde{\alpha}, h) = 4\frac{h^2}{v^2} + \frac{1}{2}\tilde{t}_0^2(\tilde{\alpha}) \left(\sqrt{\frac{h^2}{\tilde{r}_T^2(\tilde{\alpha})} + 1} + 1 \right) , \quad (5)$$

$$\text{with} \quad \tilde{r}_T(\tilde{\alpha}) = \frac{v}{4}\frac{\tilde{t}_0(\tilde{\alpha})}{\sin\tilde{\alpha}} .$$

The CRS surface shown in fig. 3 is the family of all CRP trajectories provided by all reflection points on the circle C_R and can thus be constructed with the parameters $\tilde{\alpha}$ and h. Instead of $\tilde{\alpha}$ one could also directly use a paraxial location $\tilde{x}_0$ as a parameter for the CRS surface, which can account for the case of $R_N = \infty$ that corresponds to a planar reflector in constant velocity media.

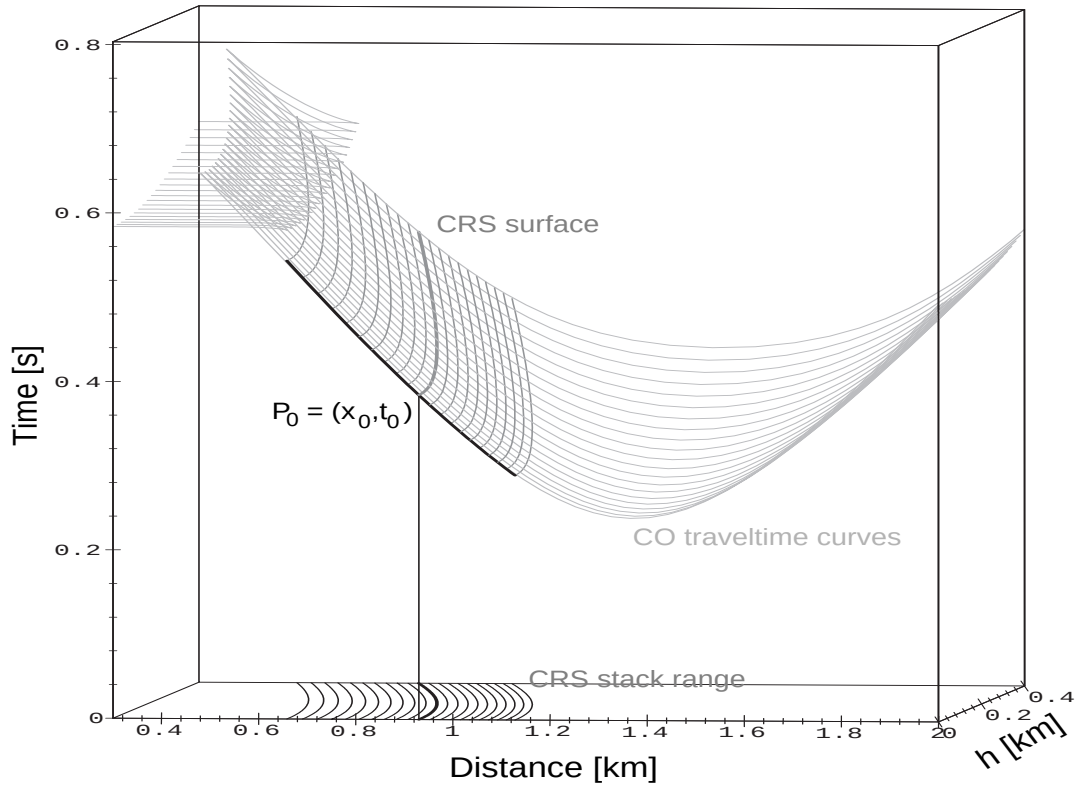

Figure 3: 3-D data space: CRS surface constructed with the CRP trajectories (dark gray) of a circular reflector. The ZO travel time curve for the circle C_R is depicted in black.

The boundaries x_{0min} and x_{0max} of the CRS surface in the ZO section of fig. 4 define the aperture in the ZO section for the CRS surface. They can be determined

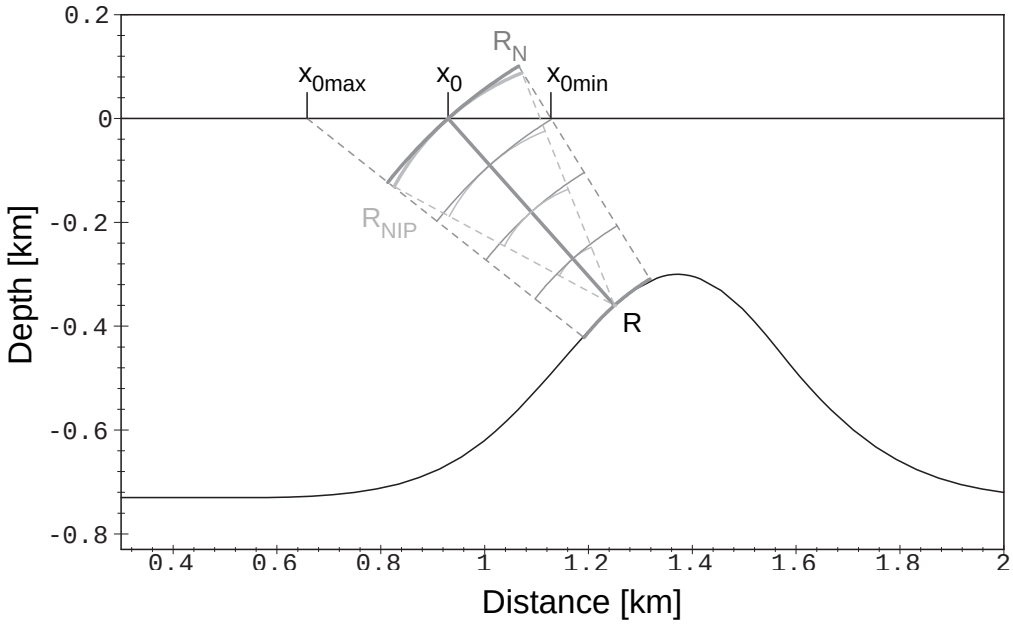

Figure 4: Constant velocity model: ZO ray and two hypothetical wavefronts that emerge at x_0 on the surface.

for instance by specifying a flare angle ($\tilde{\alpha}_{min} < \alpha < \tilde{\alpha}_{max}$). The location of all traces in the (x_m-h)-plane intersecting the CRS surface define the CRS stack range. In other words, this range is given by the projection of the CRS-surface onto the (x_m-h)-plane, i. e. by eq. (4).

Another way to provide the CRP trajectory for point P_0 is to place a fictitious point source at R. In fig. 4, a portion of the resulting circular wavefront that emerges at x_0 with radius $R_{NIP} = \frac{v}{2} t_0$ is depicted at different instants of time. We refer to this wave as *NIP* wave according to Hubral (1983). By means of this experiment the travel time for an arbitrary source/receiver pair can be determined by a double square root expression. Taking into account the dip of the reflector and Snell's law at R provides the rays and thereby the locations of the source/receiver pairs that illuminate point R on the reflector. Hence, location and travel time for a source/receiver pair are strictly determined by α and R_{NIP}. For constant velocity media the value $\tilde{R}_{NIP}(\tilde{\alpha})$ provided by other points on the circle is simply given by $\tilde{R}_{NIP}(\tilde{\alpha}) = \frac{2}{v} \tilde{t}_0(\tilde{\alpha})$.

Using the exploding reflector model for circle C_R yields the hypothetical circular wavefront emerging at x_0 with radius R_N (fig. 4). According to Hubral (1983) we refer to such a wave as *normal* wave. The purpose of using R_N instead of R_R is to express eqs. (1) and (2) with attributes (α, R_N) as expected at x_0 on the surface.

The advantage of using the attributes α, R_{NIP} and R_N will become clear later on, when we derive approximations that describe the CRS surface for inhomogeneous

media.

INHOMOGENEOUS MEDIA

Our objective is to derive formulae for the CRS stack in inhomogeneous media with constant near-surface velocity v_0. One will observe that such 2-D media can be replaced by an auxiliary homogeneous medium with the velocity v_0. Thus, we make use of the constant-velocity results above.

In order to investigate these formulae and to illustrate our assumptions we use the inhomogeneous model of fig. 5. It shows an inhomogeneous model with three constant-velocity layers and the ZO rays reflected by the dome-like structure. This structure is the same as the one in the constant velocity model, but over-lain by an additional interface. In the following, we are only interested in the reflection events of the dome-like structure and refer to it as the reflector. Furthermore, only the travel times of reflection events that pertain to this reflector are shown in the (t-x_m-h)-space. The upper interface can already be handled with the CRS stack described above.

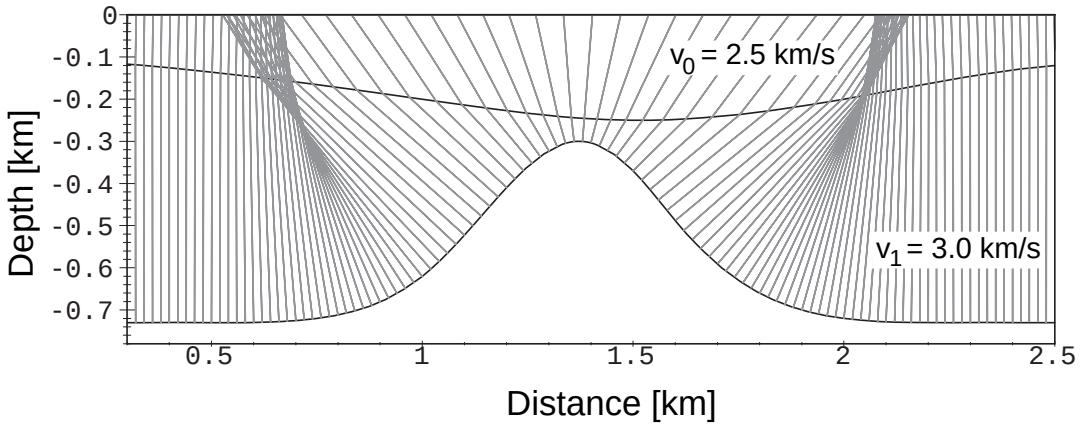

Figure 5: Inhomogeneous model: two interfaces between three homogeneous layers. The ZO rays of the dome are shown in gray.

In the following one has to clearly distinguish between concepts that have the attributes “true” and “auxiliary”. They relate to either the true or auxiliary model defined below. In fig. 6 we have plotted the true ZO ray as a bold dark gray curve connecting x_0 with R. Now, imagine a point source at R in the true velocity model that explodes at time $t = 0$. This yields a hypothetical wavefront emerging at x_0 with a specific emergence angle α and a specific radius of curvature R_{NIP}. A part of this wavefront is shown in dark gray at different instants of time in fig. 6. The emergence angle α of the *NIP* wave at x_0 coincides with the emergence angle of the ZO ray.

The attributes α and R_{NIP} observed at x_0 are sufficient to construct the circle with radius R_{NIP} centred at $R^* = (x_0 - R_{NIP} \sin\alpha, R_{NIP} \cos\alpha)$. A part of this circle is depicted in light gray in fig. 6. In other words, point R^* is defined as the center of curvature of the hypothetical wavefront that originates at point R on the true reflector and emerges at x_0 (Hoxha (1994)). The homeomorphic image (HI) of a reflector (Berkovitch et al. (1994)) is defined by all centers of curvature provided by all *NIP* waves and ZO rays of the reflector. Figure 6 shows the homeomorphic image of the reflector as light gray crosses.

The auxiliary model is defined as a medium with a constant velocity that is equal to the near-surface velocity v_0 of the true model. If one places a point source into R^* of this auxiliary model one obviously obtains a circular wavefront emerging at x_0 with the same attributes (emergence angle α and radius of curvature R_{NIP}) as would be provided by a point source at R in the true model. Since a constant velocity model is provided by the auxiliary model one can make use of these formulae by assuming the true *NIP* wave to be circular. This is a reasonable approximation in the vicinity of the central ZO ray. Replacing t_0 by $\frac{2}{v_0} R_{NIP}$ in eqs. (4) and (5) one immediately obtains the CRP trajectory for R^* in the auxiliary model. However, illuminating point R^* in the auxiliary model is not to be confused with illuminating a diffraction point: one has to take into account its dip (defined by the emergence angle α of the ZO ray), i. e. to consider it as a reflection point.

In order to obtain an appropriate approximation of the travel times for point R in the true model, one additionally has to consider that the ZO travel times for point R in the true model and point R^* in the auxiliary model will in general be different. Therefore, we make use of a time delay similar to the one introduced by de Bazelaire (1988). This time delay is simply given by the difference of the true ZO travel time t_0 and the auxiliary ZO travel time $\frac{2}{v_0} R_{NIP}$. One can also explain this time delay with the one-way travel times provided by the hypothetical experiments. There, one has to consider that both hypothetical sources at R and R^* have to explode at different times if their wavefronts are expected to arrive simultaneously at point x_0. This implies that the hypothetical source at R^* in the auxiliary velocity model should explode at $t = \frac{t_0}{2} - \frac{R_{NIP}}{v_0}$ if its counterpart, the hypothetical source in the true velocity model at R, explodes at $t = 0$.

To construct the CRS surface for point P_0 our aim is again to use CRP trajectories that pertain to a reflector segment around R. For our approximation, each CRP trajectory requires the initial values $\tilde{x}_0$, $\tilde{t}_0$, $\tilde{\alpha}$ and $\tilde{R}_{NIP}$.

Our aim is to derive formulae for these values that are independent of the macro velocity model. Therefore, we use the exploding reflector model (section) that provides the *normal* wave. The corresponding wavefront at different instants of time is shown in light gray in fig. 7. Provided that the reflector explodes at time $t = 0$, the *normal* wave emerges at time $t_0/2$ at x_0 on the surface with angle α and radius of curvature R_N. Approximating the *normal* wavefront that emerges at x_0 by a circular wavefront

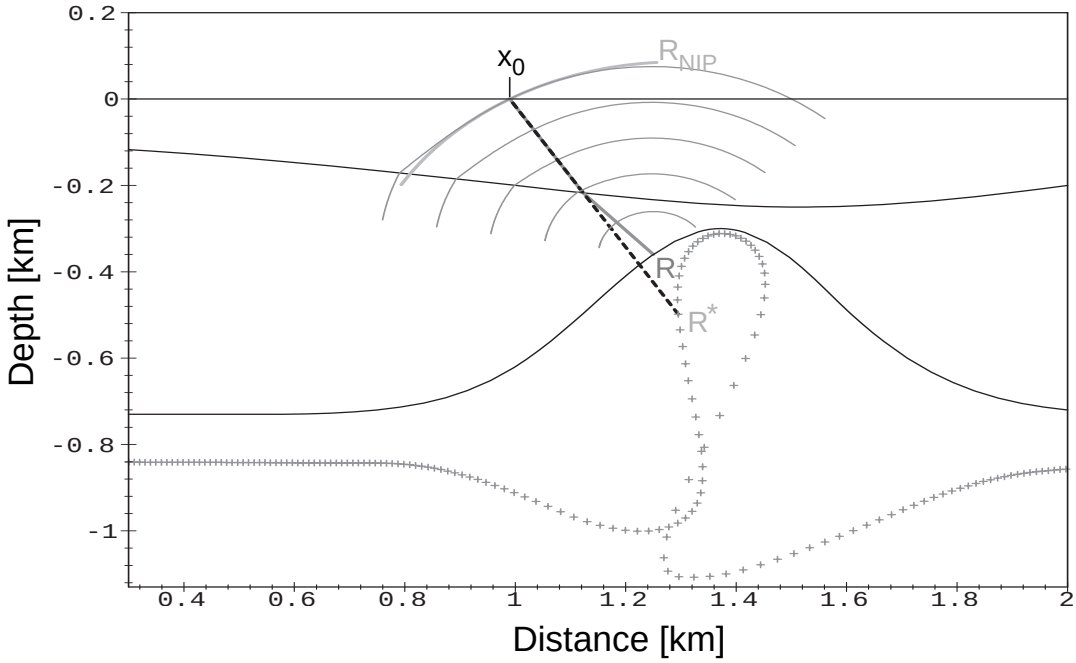

Figure 6: Inhomogeneous model: homeomorphic image (dark gray crosses) of the reflector. The wavefronts of the *NIP* wave for point R are shown at different instants of time in dark gray. The surface's influence on the *NIP* wave is not considered.

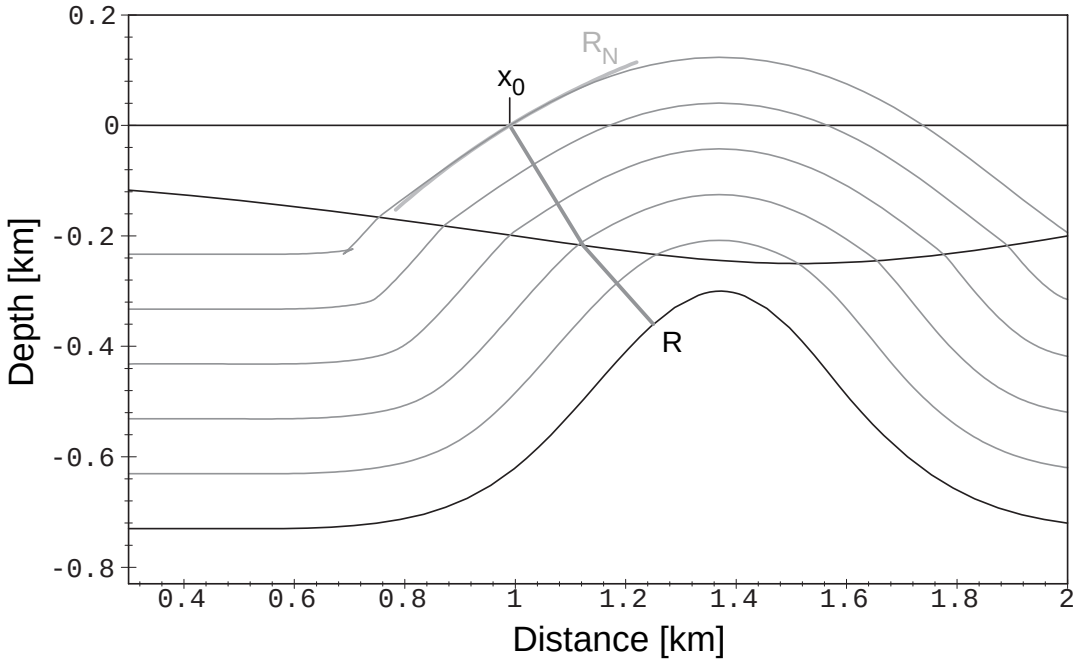

Figure 7: Inhomogeneous model: wavefronts of the *normal* wave (light gray) at different instants of time. The radius of curvature of the corresponding wavefront at x_0 is shown in dark gray. The surface's influence on the *normal* wave is not considered.

with radius R_N, we can use $\tilde{\alpha}$ as variable to specify a ZO ray and its associated CRP trajectory.[2] Thus, we want to compute the remaining initial values $\tilde{x}_0$, $\tilde{t}_0$ and $\tilde{R}_{NIP}$ in dependency of $\tilde{\alpha}$.

For the values of $\tilde{x}_0$ and $\tilde{t}_0$ this approach yields the same formulae as in the constant velocity case (eqs. (1) and (2)). However, the relationship between R_N and R_R (eq. (3)) is no longer valid. Assuming that the values of $\tilde{R}_{NIP}$ are (as the travel time $\tilde{t}_0$) constant along the circular *normal* wavefront that emerges at x_0, one can use the same approach providing $\tilde{t}_0(\tilde{\alpha})$ to determine $\tilde{R}_{NIP}(\tilde{\alpha})$ for points on the surface. The formulae for $\tilde{x}_0$, $\tilde{t}_0$ and $\tilde{R}_{NIP}$ then read:

$$\tilde{x}_0(\tilde{\alpha}) = x_0 + R_N \left(\cos\alpha \, \tan\tilde{\alpha} - \sin\alpha\right) , \tag{6}$$

$$\tilde{t}_0(\tilde{\alpha}) = \frac{2}{v_0} R_N \left(\frac{\cos\alpha}{\cos\tilde{\alpha}} - 1\right) + t_0 , \tag{7}$$

$$\tilde{R}_{NIP}(\tilde{\alpha}) = R_N \left(\frac{\cos\alpha}{\cos\tilde{\alpha}} - 1\right) + R_{NIP} . \tag{8}$$

These equations provide all initial values needed to construct the CRS surface with CRP trajectories. As stated above, one has to introduce a time delay for a CRP trajectory that accounts for inhomogeneous media. The time delay for each CRP trajectory as part of the CRS surface is given by $\tilde{t}_0(\tilde{\alpha}) - \frac{2}{v_0}\tilde{R}_{NIP}(\tilde{\alpha})$. Subtracting eq. (7) from eq. (8) yields $\tilde{t}_0(\tilde{\alpha}) - \frac{2}{v_0}\tilde{R}_{NIP}(\tilde{\alpha}) = t_0 - \frac{2}{v_0}R_{NIP}$. Hence, the approximation of $\tilde{R}_{NIP}$ yields the same time delay for all CRP trajectories that contribute to a CRS surface. The (delayed) CRS surface is then given by:

$$x_m(\tilde{\alpha}, h) = \tilde{x}_0(\tilde{\alpha}) + \tilde{r}_T(\tilde{\alpha}) \left(\sqrt{\frac{h^2}{\tilde{r}_T^2(\tilde{\alpha})} + 1} - 1\right) , \tag{9}$$

$$\left[t(\tilde{\alpha}, h) - \left(t_0 - \frac{2}{v_0}R_{NIP}\right)\right]^2 = 4\,\frac{h^2}{v_0^2} + \frac{2}{v_0^2}\,\tilde{R}_{NIP}^2(\tilde{\alpha}) \left(\sqrt{\frac{h^2}{\tilde{r}_T^2(\tilde{\alpha})} + 1} + 1\right) \tag{10}$$

$$\text{with} \quad \tilde{r}_T(\tilde{\alpha}) = \frac{1}{2}\frac{\tilde{R}_{NIP}(\tilde{\alpha})}{\sin\tilde{\alpha}} .$$

Note also that these equations reduce to the constant velocity case for $R_{NIP} = \frac{v_0}{2}t_0$.

In fig. 9 we have chosen a flare angle to determine the aperture in the ZO section (and thereby the CRS stack range). The segment of the reflector that provides ZO rays emerging in this aperture is plotted in bold black. Figure 8 shows the CRS surface constructed by means of the attributes α, R_{NIP} and R_N for point P_0.

The homeomorphic image of the reflector segment around R is marked by black crosses in fig. 9. With eq. (8) one can compute the kind of homeomorphic image that is assumed for the reflector segment around R. It is given by the circular arc segment (light gray crosses in fig. 9) with radius $R_N - R_{NIP}$ centered at $(x_0 - R_N \sin\alpha, R_N \cos\alpha)$. Assuming the *normal* wavefront to be circular in the vicinity of

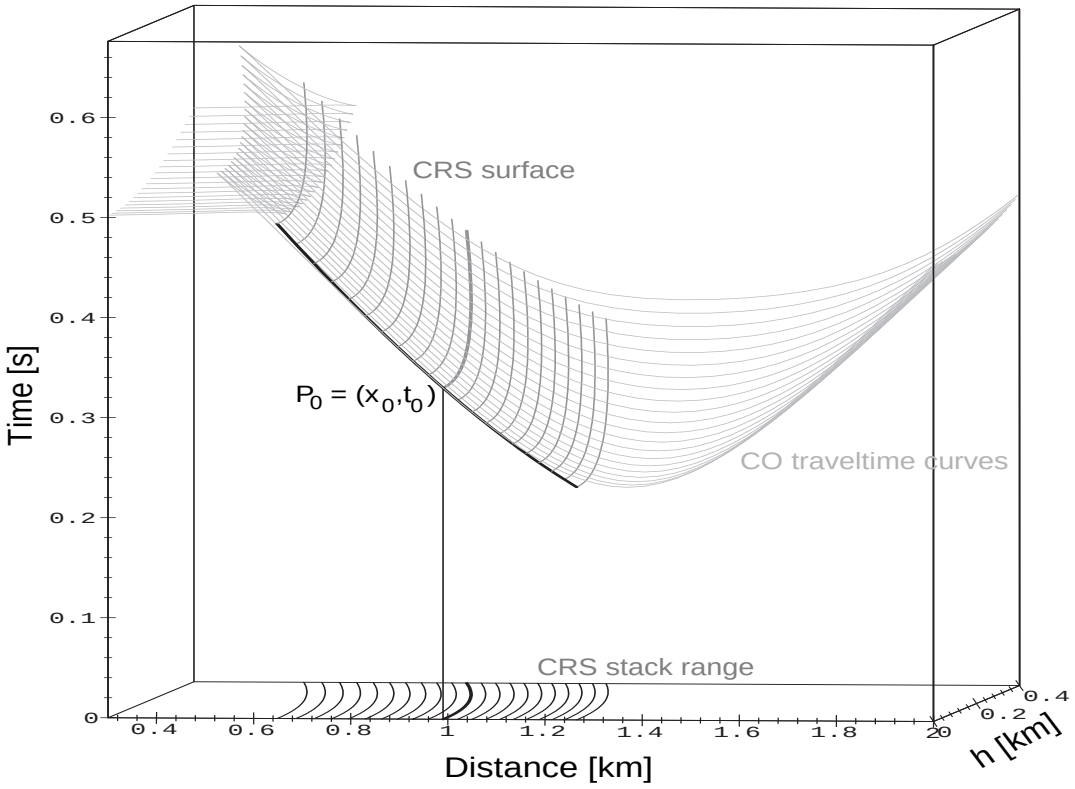

Figure 8: 3-D data space: CRS surface constructed with CRP trajectories.

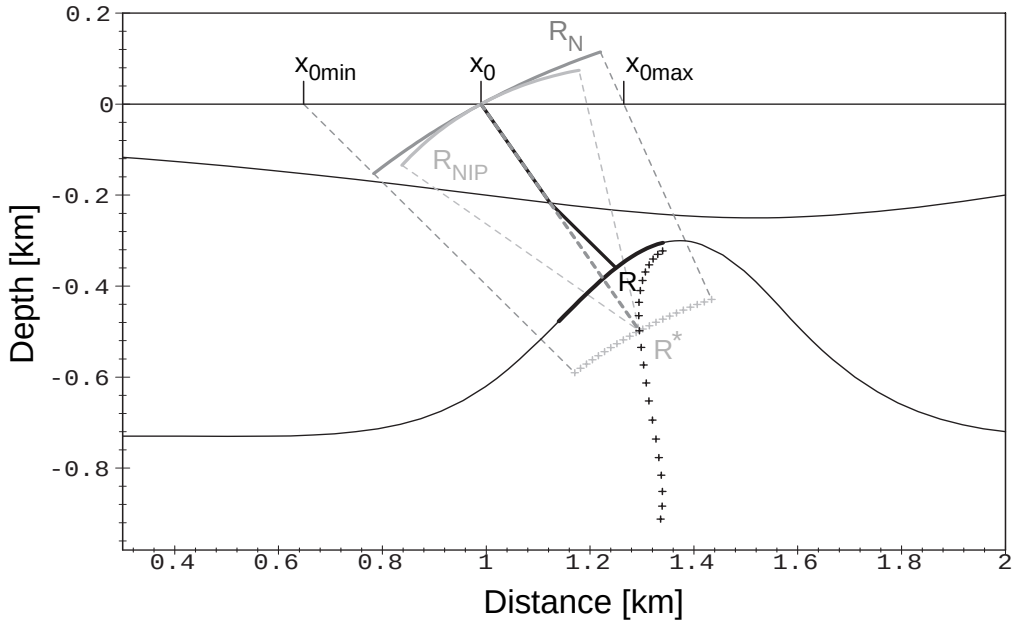

Figure 9: Inhomogeneous model: true (black crosses) and approximated (light gray crosses) HI of the black reflector segment. The approximated HI defines the circular reflector in the auxiliary model.

x_0 is a reasonable approach and is for this example confirmed by fig. 7. Consequently, the emergence angles of the true *normal* wave are well approximated by the emergence angles $\tilde{\alpha}$ of the circular wavefront. The strong deviation between the true and the assumed HI is therefore mainly due to the approximation of the values of $\tilde{R}_{NIP}$ (eq. 8).

Even if for this example eq. (8) does not provide a good approximation of the true values of $\tilde{R}_{NIP}$, some comparisons later on will show that for paraxial locations and not too large offsets the CRS surfaces provides a good approximation of the theoretical travel times.

TAYLOR-SERIES EXPANSION OF THE CRS SURFACE

In the following we provide two different Taylor expansions of the CRS surface in the (t-x_m-h)-space: one with respect to t, the other with respect to t^2. A justification for the expansion of t^2 is given by Ursin (1982), who concluded that a hyperbolic approximation is more suitable than the parabolic form. These expansions will only be performed for the CRS surface given by eqs. (9), (10) that account for inhomogeneous media. However, for the constant velocity case they reduce to the approximations of eqs. (4), (5) by substituting $\frac{v_0}{2}t_0$ for R_{NIP}. The second order expansions are given by

$$t(x_m,h) = t_0 + \frac{2\,\sin\alpha}{v_0}\,(x_m - x_0) + \frac{\cos^2\alpha}{v_0}\left(\frac{(x_m-x_0)^2}{R_N} + \frac{h^2}{R_{NIP}}\right), \qquad (11)$$

$$t^2(x_m,h) = \left(t_0 + \frac{2\,\sin\alpha}{v_0}\,(x_m - x_0)\right)^2 + \frac{2\,t_0\,\cos^2\alpha}{v_0}\left(\frac{(x_m-x_0)^2}{R_N} + \frac{h^2}{R_{NIP}}\right) \qquad (12)$$

These equations were already derived by means of paraxial ray theory and for instance formulated by Schleicher et al. (1993). In the following we will use their terminology and refer to eqs. (11) and (12) as parabolic and hyperbolic approximation, respectively. The region of convergence of these approximations depends on the chosen attributes. Later on, we will show some comparisons with the parametric CRS surface and theoretical travel times for the inhomogeneous model.

Let us now investigate formulae (11) and (12) in the CMP gather for x_0 and in the ZO section. The CMP gather is defined by the relation $x_m = x_0$. Equations (11) and (12) here reduce to

$$t(h) = t_0 + \frac{\cos^2\alpha}{v_0}\frac{h^2}{R_{NIP}}, \qquad (13)$$

$$t^2(h) = t_0^2 + \frac{2\,t_0\,\cos^2\alpha}{v_0}\frac{h^2}{R_{NIP}}. \qquad (14)$$

[2]For a planar *normal* wave one has to use $\tilde{x}_0$ as variable.

Introducing $q = \frac{cos^2\alpha}{R_{NIP}}$ shows that only one parameter q is required in the CMP gather (instead of the two attributes α and R_{NIP}).[3] The hyperbolic approximation in the CMP gather is commonly formulated by substituting v_{NMO}^2 for $\frac{2\,v_0\,R_{NIP}}{t_0\,\cos^2\alpha}$.

In the ZO section, which is specified by $h = 0$, eqs. (11) and (12) read

$$t(x_m) = t_0 + \frac{2\,\sin\alpha}{v_0}\,(x_m - x_0) + \frac{\cos^2\alpha}{v_0}\frac{(x_m - x_0)^2}{R_N}\,, \tag{15}$$

$$t^2(x_m) = \left(t_0 + \frac{2\,\sin\alpha}{v_0}\,(x_m - x_0)\right)^2 + \frac{2\,t_0\,\cos^2\alpha}{v_0}\frac{(x_m - x_0)^2}{R_N}\,. \tag{16}$$

As expected, eqs. (11) and (12) do not depend on R_{NIP} in the ZO section. This confines the search to attributes α and R_N in this section.[4]

The HIs that correspond to the parabolic and the hyperbolic approximations (eqs. (11) and (12)) in the range $\tilde{x}_{0min} < \tilde{x}_0 < \tilde{x}_{0max}$ are shown in fig. 10. The HI of the parabolic approximation (light gray circles) yields the worst result whereas the HI of the hyperbolic approximation (light gray diamonds) is close to the HI of the CRS surface.

COMPARISONS

To get an idea of the accuracy of the CRS formulae and their second order Taylor expansions, we investigate their stacking surfaces constructed for point R on the reflector in different CO sections (figs. 11 - 12). For the comparison of travel times in gathers and sections we have centred a wavelet at the theoretical travel time on each trace. The chosen wavelet is a lobe of a delayed cosine with its length equal to 10 ms. Traces that are shown in the CO sections are determined by the CRS stack range of fig. 8. The dashed light gray curve denotes the intersection of the respective CO section with the CMP gather.

Provided the circular approximations hold, one observes that the CRS surface as well as its hyperbolic and parabolic approximations show good agreements with the theoretical traveltime curves.

[3] The third order Taylor expansion reduces to the second order Taylor expansion in the CMP gather. A fourth order Taylor expansion would not reduce the number of search parameters. The influence of the fourth-order term, however, may be too small to allow a search with all parameters in the CMP gather.

[4] This already applies to the CRS surface so that there is actually no need to use a Taylor expansion in the ZO section. Here, the CRS surface can be brought into an explicit form by using $\tilde{x}_0$ instead of $\tilde{\alpha}$ as variable.

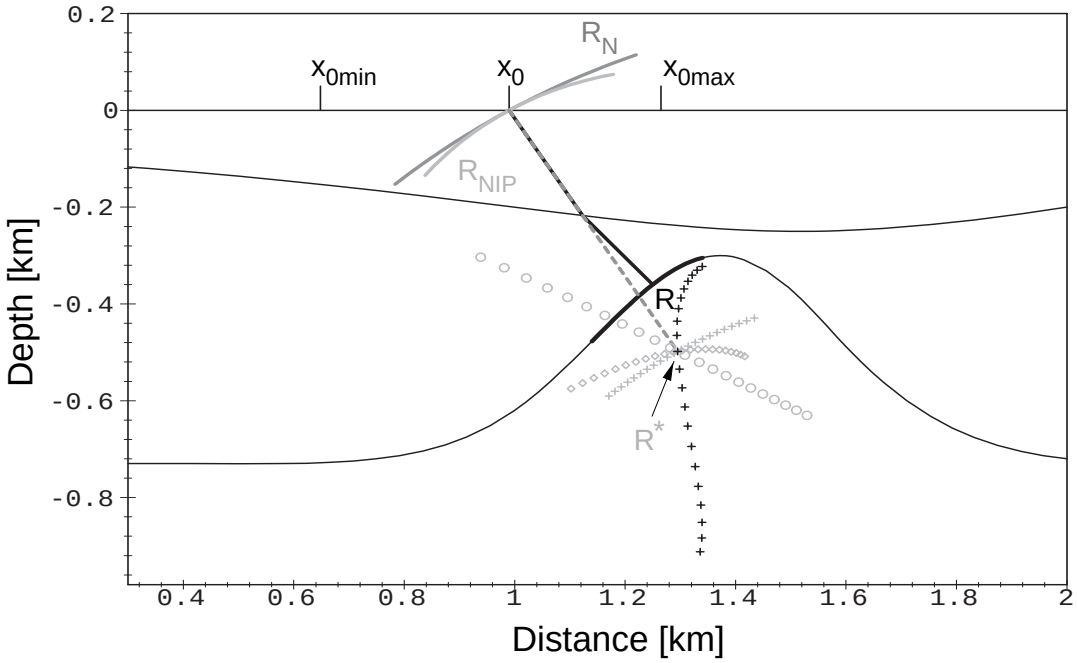

Figure 10: Inhomogeneous model: HI of the CRS surface (light gray crosses), the hyperbolic (light gray diamonds), the parabolic (light gray circles) approximations and the true HI of the reflector segment (black crosses).

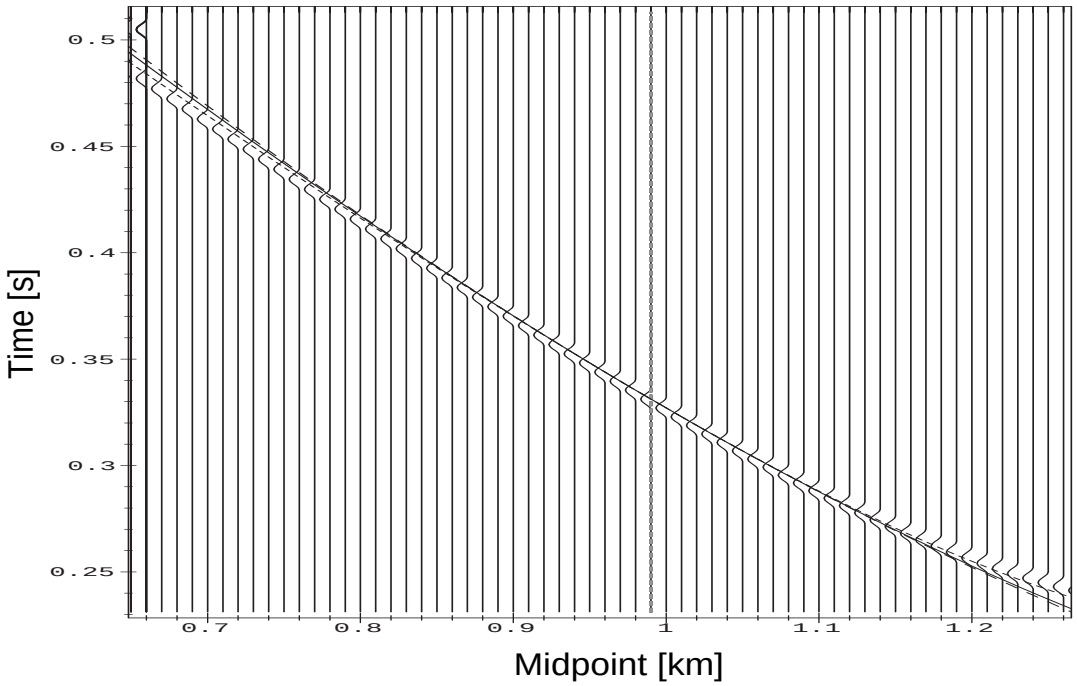

Figure 11: ZO section: the CRS surface (solid) compared to its parabolic (long dashed) and hyperbolic (short dashed) expansions in the ZO section.

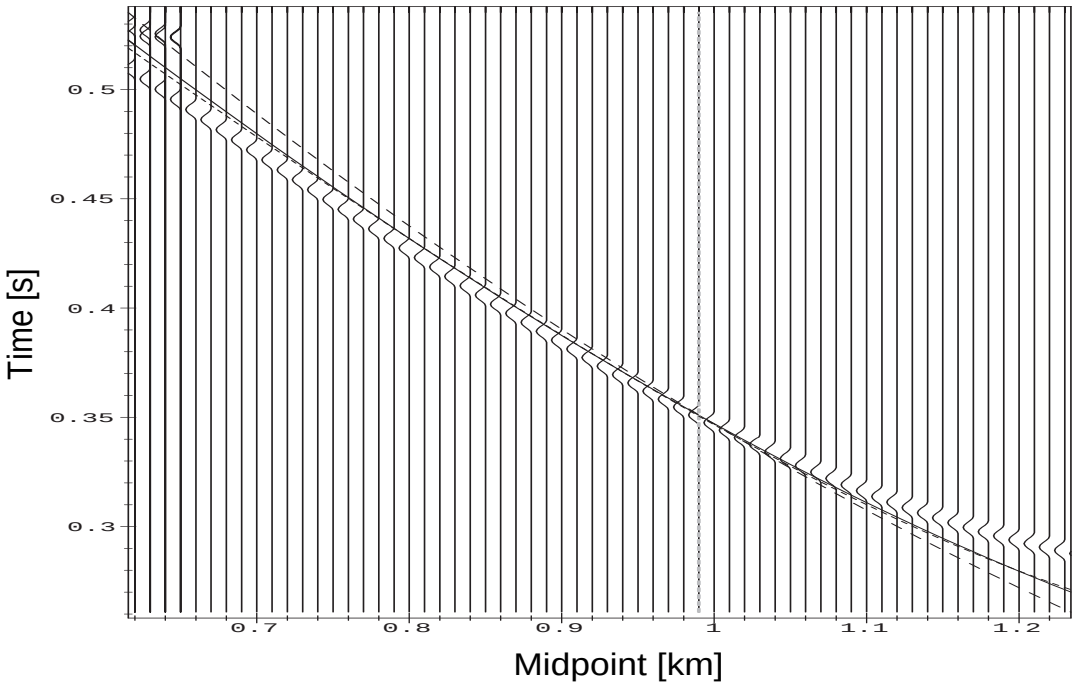

Figure 12: CO section: the CRS surface (solid) compared to its parabolic (long dashed) and hyperbolic (short dashed) expansions for a half-offset $h = 0.2$ km.

CONCLUSION

The CRS stack is a model independent seismic imaging method and thereby can be performed without any ray tracing and macro velocity model estimation. As a result of a CRS stack one obtains in addition to each simulated ZO reflection time important wave-field attributes: the angle of emergence and the radii of curvature of the *NIP* and the *normal* wave. These attributes can subsequently be used to derive an approximation of the inhomogeneous 2-D macro velocity model (Hubral and Krey (1980), Goldin (1986)) which allows to determine an image in the depth domain.

By means of the Taylor series expansions, the CRS stack can be applied to traces on an arbitrarily irregluar grid without the need to interpolate. Additionally, the simulated ZO section and the attribute sections are not restricted to the (possibly irregular) input data geometry.

REFERENCES

Berkovitch, A., Gelchinsky, B., and Keydar, S., 1994, Basic formulae for multifocusing stack: 56th Mtg. Eur. Assoc. Expl Geophys., Extended Abstracts, Session:

P140.

Black, J. L., Schleicher, K. L., and Zhang, L., 1995, True-amplitude imaging and dip moveout:, *in* DMO processing Soc. Expl. Geophys., 448–467.

de Bazelaire, E., and Thore, P., 1987, Pattern recognition applied to time and velocity contours: 57th Annual Internat. Mtg., Soc. Expl. Geophys., Expanded Abstracts, Session: POS2.14.

de Bazelaire, E., and Viallix, J. R., 1994, Normal moveout in focus: Geophys. Prosp., **42**, no. 5, 477–499.

de Bazelaire, E., 1986, Normal moveout revisited – inhomogeneous media and curved interfaces: 56th Annual Internat. Mtg., Soc. Expl. Geophys., Expanded Abstracts, Session: POS2.4.

de Bazelaire, E., 1988, Normal moveout revisited – inhomogeneous media and curved interfaces: Geophysics, **53**, no. 2, 143–157.

Gelchinsky, B., 1988, The common-reflecting-element (CRE) method: ASEG/SEG Internat. Geophys. Conf., Expl. Geophys., Extended Abstracts, 71–75.

Goldin, S. V., 1986, Seismic traveltime inversion: Soc. Expl. Geophys., Tulsa.

Höcht, G., Perroud, H., and Hubral, P., 1997, Migrating around on hyperbolas and parabolas: The Leading Edge, **May**, 473–476.

Hoxha, F., 1994, Fonctions de Green et migration de Kirchhoff par imagerie optique: Ph.D. thesis, Université de Pau.

Hubral, P., and Krey, T., 1980, Interval velocities from seismic reflection traveltime measurements *: Soc. Expl. Geophys.

Hubral, P., Schleicher, J., and Tygel, M., 1996a, A unified approach to 3-D seismic reflection imaging, Part I: Basic concepts: Geophysics, **61**, no. 3, 742–758.

Hubral, P., Tygel, M., and Schleicher, J., 1996b, Seismic image waves: Geophys. Journ. Intern., **125**, 431–442.

Hubral, P., Höcht, G., and Jäger, R., 1998, A new look at subsurface illumination in seismic imaging: Submitted to The Leading Edge.

Hubral, P., 1983, Computing true amplitude reflections in a laterally inhomogeneous earth: Geophysics, **48**, no. 8, 1051–1062.

Keydar, S., Gelchinsky, B., Shtivelman, V., and Berkovitch, A., 1990, The common-evolute-element (CEE) stack imaging: 60th Annual Internat. Mtg., Soc. Expl. Geophys., Expanded Abstracts, 1911–2013.

Schleicher, J., Tygel, M., and Hubral, P., 1993, Parabolic and hyperbolic paraxial two-point traveltimes in 3D media: Geophys. Prosp., **41**, no. 4, 459–513.

Taner, M. T., and Koehler, F., 1969, Velocity spectra – digital computer derivation and applications of velocity functions *: Geophysics, **34**, no. 6, 859–881.

Tygel, M., Schleicher, J., and Hubral, P., 1996, A unified approach to 3-D seismic reflection imaging, Part II: Theory: Geophysics, **61**, no. 3, 759–775.

Ursin, B., 1982, Quadratic wavefront and traveltime approximations in inhomogeneous layered media with curved interfaces: Geophysics, **47**, no. 7, 1012–1021.